
PHASE
TRANSITIONS

Phase Formation and Conductivity Fluctuation Investigation in Nanoparticle SnO₂-Added Y₃Ba₅Cu₈O_{18 ± δ} Polycrystalline Superconductor

N. Ghaedsharafi^a, G. Shams^{a,*}, and Z. Soltani^a

^a Department of Physics, Shiraz Branch, Islamic Azad University, Shiraz, Iran

* e-mail: shams@iaushiraz.ac.ir

Received May 23, 2020; revised May 23, 2020; accepted May 29, 2020

Abstract—The influence of 0, 0.20, 0.40, 0.50, and 0.60 wt % nano-sized tin oxide (SnO₂) particles on electrical conductivity fluctuation in normal and superconducting state of the Y₃Ba₅Cu₈O_{18 ± δ} (denoted as Y-358) polycrystalline samples is studied. Phase formation and microstructures have been systematically examined. By increasing the content of SnO₂ in YBCO matrix, X-ray diffraction technique showed slight variation in lattice parameters and overall reduction in the orthorhombicity. Scanning electron microscopy observations and the crystallite size calculation also revealed that the grain size and the average crystallite size decreased compared to the SnO₂-free sample. Aslamazov–Larkin and Lawrence–Doniach prototypes were used to analyze conductivity fluctuations based on the electrical resistivity $\rho(T)$ measurements. Superconducting transition temperatures T_C and T_{LD} have been reported. The influence of SnO₂ addition on the superconducting properties indicates that with the addition of SnO₂ nanoparticles into Y-358 compound, some parameters values such as zero-resistance critical temperature $T_{C\text{ zero}}$, coherence distance alongside the c axis at 0 K $\xi_c(0)$, and super-layer length d decrease in total, while anisotropy γ , critical magnetic fields $B_{c1}(0)$, $B_{c2}(0)$, and critical current density $J_c(0)$ increase in SnO₂-added Y-358 specimens compared to the pure one. The reasons corresponding to these scenarios are discussed in details.

Keywords: phase formation, conductivity fluctuation, SnO₂ nanoparticle, Y-358

DOI: 10.1134/S1063783420110141

1. INTRODUCTION

Thermal fluctuations have been detected in all low-temperature superconductors (LTSCs) and high-temperature superconductors (HTSCs). Investigation on HTSCs concerning the fluctuation phenomena leads to a significant understanding of dynamic mechanism in these materials. Thermal fluctuation is responsible for establishment of superconductivity by Cooper pairs beyond T_C which is commenced about $2T_C$. Increasing the Cooper pairs number occurs promptly at the cost of the ordinary electrons which creates fluctuation conductivity throughout the carriers transportation [1, 2]. The analysis of fluctuation-induced electrical conductivity traces to three different influences, so-called the density of states (DoS) and the Aslamazov–Larkin (AL) and Maki–Thompson (MT) expressions. The first term is associated with the reordering of the positions nearby the Fermi energy; meanwhile, electrons involved in pair transportation are inaccessible for a solitary charge transport. In the next one, the creation of Cooper pair results in an equivalent superconducting passage in the non-superconducting stage; lastly, the third expres-

sion considers the articulate dispersion of contaminations of the interrelating electrons. Very close to the T_C , the differing performance of the DoS expression is cut off by the MT correction that has opposite sign, while the AL and MT expressions both hint to an improvement of the conductivity above T_C [3].

Superconductor properties can be improved by adding some variety of impurities with nano-size particles. These noticeable improvements are being detectable in YBCO family compounds when they mix with Mn₃O₄, Y₂Cu₂O₅, and Ag nanoparticles [4–6]. However, manipulating and controlling superconductors with nano-sized doping might result in unanticipated modifications of the behavior of these materials [7].

Specific impurities such as tin and tin oxide are often presented partial to YBCO slim layers made up by metallic deposition procedure. These resources construct Sn-based nanoparticles in the superconductors system that can show by way of actual pinning regions [8–10]. Constant spread of tin-founded responded phase was similarly detected while adding tin-oxide into melt texture growth polycrystalline

$Y_1Ba_2Cu_3O_{7-\delta}$ (noted MTG Y-123) [11]. The most recent research in the micro-organization and characteristics of Y123 superconductors manufactured through the thermal behavior technique and by the addition of $x = 0, 0.4, 0.8,$ and 1.0 wt % SnO_2 nano-sized particles showed that the compound with $x = 0.4$ SnO_2 inclusion demonstrated the greatest superconducting parameters amongst the specimens [12].

In this research for the first time after the similar impetus as earlier research, attempts have been made to investigate the essential evaluation consistent with varied amount of $x = 0-0.60$ wt % SnO_2 nanoparticles (35–55 nm) inclusions additional to the $Y_3Ba_5Cu_8O_{18\pm\delta}$ superconductor samples that are fabricated by conventional solid-state response process. For determination of specific inconsistencies in doped and pure composites Aslamazov–Larkin (AL) concept and Lawrence–Doniach (LD) theory were appropriate tools to examine the performance of thermal instabilities conductivity beyond the T_C . We found T_{LD} , $\xi_c(0)$, and d that are, respectively, boundary temperature at the transition from three-dimensional to two-dimensional, the coherence length alongside the c -axis when the temperature approaches 0 K, and effectual super layer length associated with the two-dimensional classification. Soon after computing the anisotropy γ and the interlayer pairing J , related to our superconductors, also at the zero-temperature condition and the critical current density, thermodynamic, the lower and the upper critical magnetic fields labeled $J_c(0)$, $B_c(0)$, $B_{c1}(0)$, and $B_{c2}(0)$ were calculated correspondingly.

2. EXPERIMENTATION DETAILS

Nanopowder of tin oxide with chemical formula SnO_2 , purity level 99.7%, and nano-size 35–55 nm was prepared from US Research Nanomaterials, Inc. located in Houston, TX, USA. The tin-oxide nanoparticles have been produced from clean chemical substance and rinsed by purified water. Transmission electron microscopy (TEM) has shown its morphology shape is spherical, with true density of 6.95 g/cm³, the average particle size (APS) of 35–55 nm, with white colour and purity better than 99.5%. Doped samples with SnO_2 nanoparticles and pure $Y_3Ba_5Cu_8O_{18\pm\delta}$ were prepared by conservative solid-state response technique. The powders through chemical formulation CuO , Ba_2CO_3 , and Y_2O_3 with high quality and 99.9% purity (Merck, Germany) were used to manufacture YBCO polycrystalline and mixed at a ratio of Y : Ba : Cu = 3 : 5 : 8. The hard-pressed pellets were made of the assorted materials and subsequently underwent calcination cycle during 12 h at 900°C. This procedure was repeated once more with medium grinding. During the final processing stage, SnO_2 nano-sized elements were added to the foundation powders of Y-358 by crushing and mixing in an

agate mortar. The added quantity of SnO_2 was assorted from $x = 0$ to 0.60 wt % of the entire amount of the specimen. The pressure applied to the mixture grinds in pellets was about 200 bar to form round disks with dimensions of 30×4 mm. The samples were enclosed to quartz crystal pipe, and the sintering process was performed at 950°C with 48-h duration in the vicinity of flowing oxygen, with consequently tranquilizing to 25°C at a rate of 4°C/min. After preparing pure Y-358 samples and doped with SnO_2 nanoparticles inclusion, X-ray diffraction (XRD), scanning electron microscope (SEM), and resistivity measurements were investigated to evaluate the phase formation, lattice parameters, the oxygen content, microstructures, and conductivity fluctuations. More details about these issues can be found in [6]. Segmentation techniques are used and followed by generating a binary image to exhibit SEM images at more clarity. In fact, by segmenting an image each pixel can only have one of two values to indicate whether it is part of an object or not. The conventional method to generate a binary image is the thresholding fashion in which image pixels intensity is identified below (min) or above (max) particular threshold values so that only pixels falling within a specified range are detected. Therefore, those of pixels intensity values above the threshold pointed to a foreground (desirable objects) whereas all the remaining values contributed to a background.

3. EXCESS CONDUCTIVITY STUDY

Aslamazov–Larkin (AL) concept [13] that describes the conductivity fluctuation beyond critical temperature is used by the following formula:

$$\Delta\sigma = A\varepsilon^{-\nu}. \quad (1)$$

Here, A and ν are named AL constant and Gaussian analytical exponent, respectively. The latter is reliant on the dimensionality of superconducting scheme while ε symbolizes the reduced temperature as follows:

$$\varepsilon = \ln\left(\frac{T}{T_c^p}\right). \quad (2)$$

According to the Gauss–Ginzburg–Landau (GGL) approach, $\varepsilon \ll 1$ and by means of the following approximation for the reduced temperature, frequently used in the Aslamazov–Larkin theory

$$\varepsilon = \ln(T/T_c^p) \cong (T - T_c^p)/T_c^p, \quad (3)$$

where T_c^p is the temperature correlated to the peak obtained from dp/dT .

Pertinent to the AL model [13] and in the mean-field area by deducting the backdrop normal-state conductivity from the self-possessed conductivity, the fluctuation-induced conductivity $\Delta\sigma$ is generally expressed as follows [14]:

$$\Delta\sigma = \sigma_m(T) - \sigma_n(T), \quad (4)$$

where $\sigma_m(T)$ and $\sigma_n(T)$ categorize the measured and normal conductivity, respectively, which is extrapolated above $2T_C$. $\sigma_n(T)$ is computed in the presumption of a linearized or a Zou–Anderson requirement for conductivity $\sigma(T) = 1/\rho(T)$. The following equation demonstrates relationship between D the dimensionality arrangement and ν the Gaussian analytical exponent,

$$D = 2(2 - \nu). \quad (5)$$

The Gaussian critical exponent ν which is a parameter dependent on D , designates with double parts:

(1) For 3D part associated with $\nu = -0.5$ and $A = A_{3D}$ we can write:

$$\Delta\sigma = A_{3D}\varepsilon^{-0.5}, \quad (6)$$

where $A_{3D} = \frac{e^2}{32\hbar\xi_c(0)}$ and $\xi_c(0)$ shows coherence length in c direction of multilayer structure at 0 K.

(2) For 2D contribution when $\nu = -1$ and $A = A_{2D}$, then the excess conductivity can be written as

$$\Delta\sigma = A_{2D}\varepsilon^{-1}, \quad (7)$$

where $A_{2D} = \frac{e^2}{16\hbar d}$ and d is the periodicity length of superconducting layers. These effective ν values for 3D and 2D contribution defined paraconductivity fluctuation [15]. However, the graphs of $\ln(\Delta\sigma)$ versus $\ln(\varepsilon)$ for none-added and doped Y-358 accomplish resolution of the explainer values. These values can be obtained from the slopes of linear fitting to link investigational numbers with theoretically expected data. In Gaussian fluctuations region if the plots consist of three distinct regimes, another contribution may be introduced as follows:

(3) For 1D contribution associated with $\nu = -1.5$ and $A = A_{1D}$, we can write:

$$\Delta\sigma = A_{1D}\varepsilon^{-1.5}, \quad (8)$$

where $A_{1D} = \frac{e^2\xi_c(0)}{32\hbar\omega}$ and ω is the wire cross-sectional zone related to the 1D scheme. According to layered superconductors and Lawrence–Doniach context [16], the analysis of the fluctuation conductivity above the mean critical transition temperature T_C^P were performed because the excess conductivity occurs in the layers of superconductors joined by Josephson tunneling

$$\Delta\sigma = A \frac{\sqrt{\varepsilon(\varepsilon + J)}}{\varepsilon(\varepsilon + J)}. \quad (9)$$

$A_{2D} = \frac{e^2}{16\hbar d}$ is named the temperature-independent amplitude while J is named the coupler among the

superconductors layers which is constant and defined by

$$J = \left(\frac{2\xi_c(0)}{d} \right)^2. \quad (10)$$

Here, $\xi_c(0)$ is the coherence length alongside c -axis at 0 K and d is defined as the interlayer placing. In weak-link situation when $J \ll 1$, Eq. (9) decreases to the 2D expression. The 3D term is obtained in the condition $J \gg 1$. For YBCO specimens, the Lawrence–Doniach principle [17] was used to find the $\xi_c(0)$ at the change-over temperature, T_{3D-2D} :

$$T_{2D-3D} = T_C^P(1 + J). \quad (11)$$

The anisotropy γ related to layered superconductor classifications was specified by way of [18]:

$$\gamma = \frac{\xi_{ab}(0)}{\xi_c(0)}, \quad (12)$$

where $\xi_{ab}(0)$ is the consistency distance in the direction perpendicular to c axis with its value between 10 and 20 Å associated with YBCO [17]. The Ginzburg number can be determined experimentally as

$$N_G = \left| \frac{T_G - T_C}{T_G} \right| = \frac{1}{2} \left(\frac{k_B T_C \gamma}{B_c^2(0) \xi_c^3(0)} \right)^2 = \frac{1}{2} \left(\frac{k_B}{B_c^2 \gamma^2 \xi_c^3(0)} \right)^2, \quad (13)$$

where T_G , T_C , and k_B are the temperature due to ending three dimensionality system, critical temperature, and the constant of Boltzmann, respectively. However, the critical field at zero temperature $B_c(0)$ can be assessed as follows:

$$B_c(0) = \frac{\Phi_0}{\sqrt{8\pi\lambda(0)\xi_c(0)}}. \quad (14)$$

In this equation, Φ_0 and λ_0 are called fluxion and penetration depth, correspondingly. The lower and upper critical magnetic fields $B_{c1}(0)$ and $B_{c2}(0)$ accompanied with critical current density $J_c(0)$ are computed by implementation the value of $B_c(0)$ and λ_0 into the GL equations:

$$B_{c1} = \frac{B_c \ln k}{\sqrt{2}k}, \quad (15)$$

$$B_{c2} = \kappa B_c \sqrt{2}, \quad (16)$$

where k is proportion of λ to ξ and entitled the Ginzburg–Landau parameter and eventually J_c is computed as follows:

$$J_c = \frac{4\kappa B_{c1}}{3 \ln \kappa \sqrt{3}\lambda}. \quad (17)$$

4. RESULTS AND DISCUSSION

The X-ray diffraction graphs associated with none-added specimens Y-358 and doped through varied quantities of $x = 0-0.060$ wt % SnO₂ nanoparticles

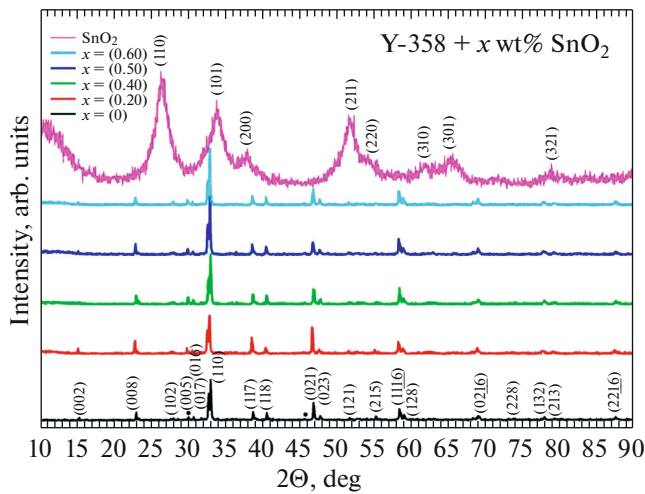


Fig. 1. XRD graphs of the powder's specimens due to untainted Y-358 and doped SnO₂ nano-sized inclusions. The character (•) represents Y-211 as subordinate phases.

accompanied with the pure SnO₂ nanopowder are illustrated in Fig. 1.

The XRD analysis of the samples show that their space group symmetry and structure phase are *Pmm2* and orthorhombic, respectively. From X-ray designs, 20 diffraction peaks are obvious along 2θ axis corresponding to crystalline flat surfaces of Y₃Ba₅Cu₈O_{18±δ}. Most of the peak positions are in a good agreement with Y-358 [19]. Cumulative effect of the SnO₂ inclusion on the growth of crests implies that the higher SnO₂ doping results in better granules. This influence can be seen apparently about the peak at 32.63° particularly with $x = 0.50$ and 0.60 wt %, which enunciates the same discussion with other literature [20]. More peaks also exist in the pattern within 29° to 46°, matching Y-211 phase related to the samples. According to SnO₂ nanoparticles, the peaks are linked to (110), (101), (200), (211), (220), (310), and (301) (Miller's Indexes). These indexes corroborate that SnO₂ nanoparticles with tetragonal structure, and lattice parameters of $a = 4.73820$ Å, $b = 4.73820$ Å, and $c = 3.18710$ Å are harmonized by JCPDS card no. 41-1445. Scherrer equation [21] was used to calculate the average crystallite size Z :

$$Z = \frac{C\lambda_{Cu}}{L \cos \theta}, \quad (18)$$

where C is defined as form factor excluding any dimension (~ 0.89), λ_{Cu} has presented the wavelength of X-ray radiation with the value ~ 0.15418 nm, L is the line full width at half-maximum in radian and θ is Bragg angle at the peaks. Five peaks at 2θ values of 22.8349567°, 32.58549785°, 32.82142855°, 38.538961°, and 46.6619048° were chosen to obtain the crystallite size. The average crystallite size was found to be 50.32623, 44.65428, 46.63808, 51.63545, and

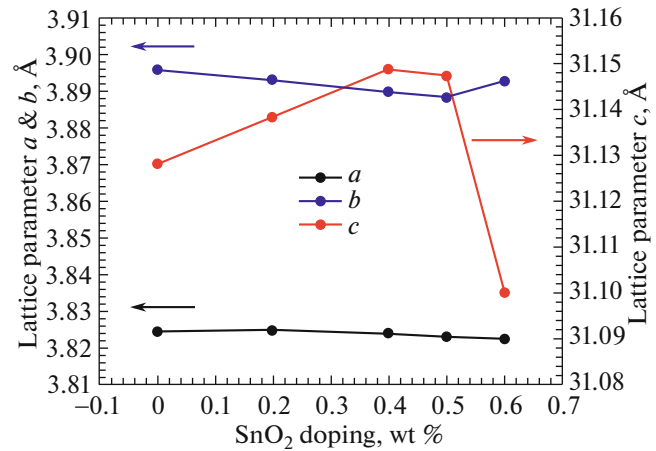


Fig. 2. Variant of unit cell dimensions a , b , and c related to Y-358 specimens doped by different quantities of SnO₂ nanoparticles.

48.48951 nm, for $x = 0, 0.20, 0.40, 0.50,$ and 0.60 , respectively.

There are no substantial modifications related to the X-ray diffraction patterns with adding SnO₂, excepting on behalf of very tiny peaks at 51.8°, and it is hardly to say these peaks can be associated with SnO₂ addition, because they may be overlapped with the base peaks of Y-358 in X-ray diffraction patterns. According to Y-123, some works found extra small peaks associated with the addition of SnO₂ nanoparticles (e.g. [12]). These peaks can be allocated to BaSnO₂ related to Y-123 [10, 22], while other indicates belong to Y–Ba–Sn–O [9]. However, our results show that adding a small quantity of SnO₂ within the specimen does not noticeable affect the last outcome into the XRD determination and obviously, in the X-ray curving designs lack of any peak consistent with the Sn-based mixes is evident.

Figure 2 shows so-called lattice parameters a , b , and c for pure and SnO₂ nanoparticles doped samples listed in Table 1.

Materials analysis using diffraction (MAUD) software based on the Rietveld refinements was used to determine the lattice parameters. Values of a , b , and c related to the non-doped specimen are 3.8245595, 3.8955772, and 31.128101 Å, correspondingly. These data for Y-358 are in agreement with reported before [23–26]; whereas c agrees with others [27, 28]. However, comparing Y-358 to Y-123 regarding a and b parameters shows that the similarity is apparent [27] but in the case of c parameter, for Y-123 it is nearly one third of Y-358 [27, 29]. Adding SnO₂ falls out in an almost constant parameters a and b but a growth in c with doping increase up to $x = 0.50$. The higher c parameter might stand trustworthy for a poorer inter-layer junction and so would be liable for worse quali-

Table 1. Lattice constants of Y-358 specimens by various quantities of SnO₂ nano-sized inclusion

Y-358+ <i>x</i> wt % SnO ₂					
Parameters	<i>x</i> = 0	<i>x</i> = 0.20	<i>x</i> = 0.40	<i>x</i> = 0.50	<i>x</i> = 0.60
<i>a</i> , Å	3.8245595	3.8247192	3.8238554	3.8229556	3.82242
<i>b</i> , Å	3.8955772	3.8927503	3.8898766	3.8883142	3.8926938
<i>c</i> , Å	31.128101	31.138376	31.148827	31.147375	31.100006
Volume of cell, Å ³	463.77343	463.60922	463.3178	463.00114	462.75287
Average crystallite size, nm	50.32623	44.65428	46.63808	51.63545	48.48951
Oxygen content	17.68744	17.69783	17.71806	17.72486	17.67508
Calculated density, g/cm ³	4.39426	4.7794	4.61165	4.17922	4.62057

ties of superconductors [30]. The last doping $x = 0.60$ causes sudden decrease of c parameter. Doping level of some elements such as Co and Fe performs differently when inserted into the YBCO samples: for low-level doping, they are mainly detected at the Cu(I) location and for high-level, they settle at the Cu(II) position [31, 32]. Our results show that the c lattice parameter discrepancies is less than 0.15% while a and b are almost constant by the addition of SnO₂ nanoparticles. However, by inclusion the low doping level (up to $x = 0.60$ wt %) of SnO₂ nanoparticles, unimportant modifications related to a , b , and c happened, causing that tin did not unify with crystal structure, but instead most probably contributed into the shape of tin-based subordinate phases.

This is an adequate signal that the replacement of tin is not traceable in the Y-358 structure which is supported by other literatures associated with the Y-123 system [12, 33, 34].

Volume of cells obtained by multiplication of unit cell dimensions (abc) accompanied with the average crystallite size and also calculated density for all composites ($x = 0$ to 0.60 wt %) are recorded in Table 1.

The calculated densities of Y₃Ba₅Cu₈O_{18±δ} specimens with SnO₂ nanoparticles doping ($x = 0, 0.20, 0.40, 0.50,$ and 0.60 wt %) are 4.39426, 4.7794, 4.61165, 4.17922, and 4.62057 g/cm³, respectively. The data indicate that as compared with SnO₂-free sample, by increasing nano-SnO₂ inclusions, the density of YBCO samples increase ($x = 0.50$ wt % is exceptional), and this progression is involved in an association concerning estimated density and the total of passageway in superconductors so that these aspects increase together with raising nano-sized inclusion, which can be approved by other research [35]. Orthorhombicity $Y = (b - a)/(b + a)$ and oxygen content of the Y-358 phase are depicted in Fig. 3.

The oxygen contents are estimated to be 17.68744, 17.69783, 17.71806, 17.72486, and 17.67508 belonging to add-free and tin-oxide doped specimens associated with assorted impurities ($x = 0$ to 0.60) Y₃Ba₅Cu₈O_{18±δ} + x wt % SnO₂, correspondingly, and are also placed in

Table 1. According to Fig. 3, the differentiation concerning a and b declines through adding SnO₂ nanoparticles up to 0.50 wt % that can be interpreted as the decrease in orthorhombicity regarding the pure composite with higher orthorhombicity, which has been similarly reported in other paper for Ag-doped samples [36].

From 0.20 to 0.50 wt % SnO₂ doping, the values of orthorhombicity decrease while the oxygen content increased in all cases except for $x = 0.60$ wt % sample. Meanwhile, with nanoparticles dispersed throughout the sample, the orthorhombicity Y is related to oxygen content and reduces by rising SnO₂ doping. Although, our results indicated that increasing tin oxide nanoparticles doping triggered upsurge of the oxygen substance, the properties of high temperature superconductors, particularly YBCO family, are correlated to the O element, the arrangement of O atoms, and their opening situations in the copper–oxygen plane.

Figure 4 illustrates the electrical resistivity measurement for none-added Y₃Ba₅Cu₈O_{18±δ} polycrystal-

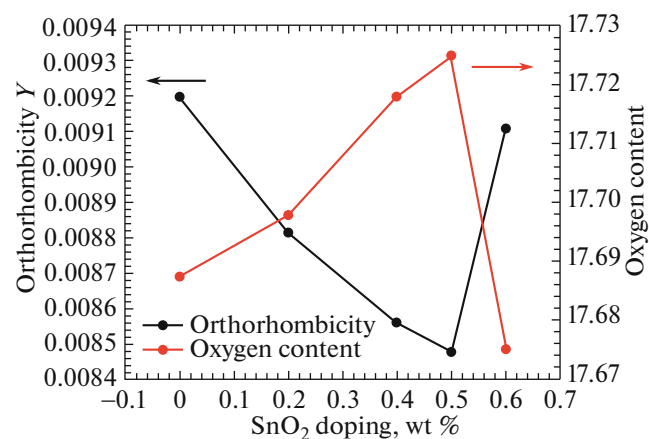


Fig. 3. The orthorhombic distortion Y and oxygen content for Y-358 compounds mixed through different weight of SnO₂ nanoparticles.

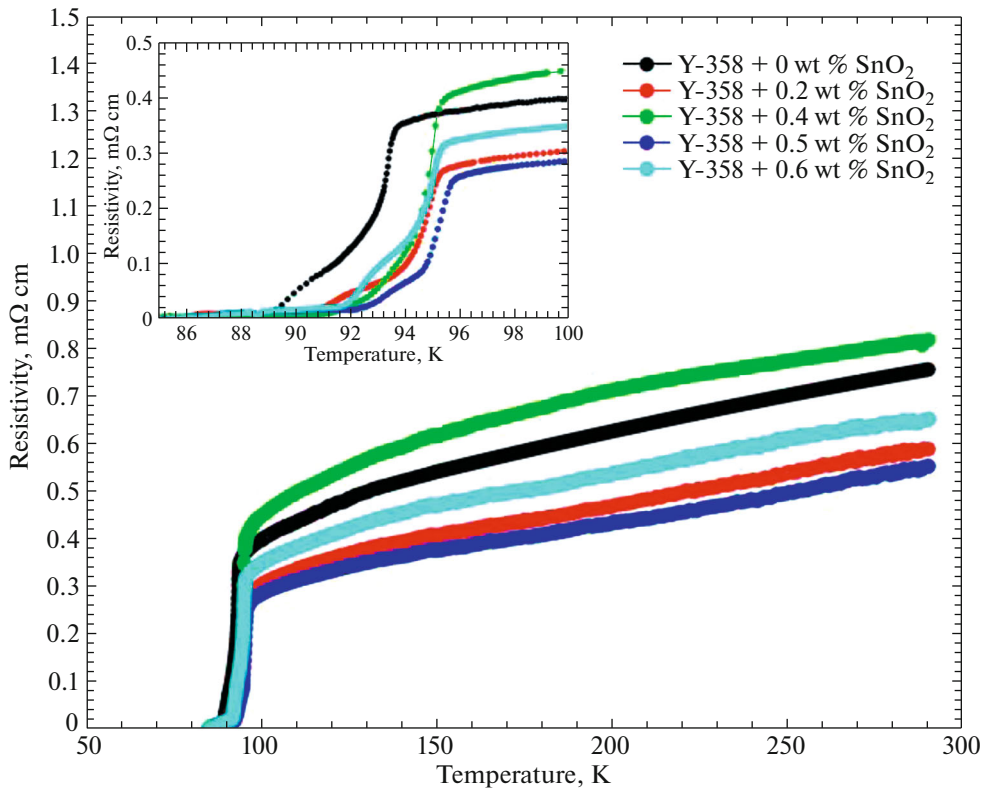


Fig. 4. Plots of resistivity against temperature of the polycrystalline Y-358 + x wt % SnO₂ nanoparticle doped ($x = 0, 0.20, 0.40, 0.50,$ and 0.60) samples. Inset: Specific section of the graph exhibiting accurate T_{C0} and T_C .

line superconductor and SnO₂ nano-sized addition to Y-358 specimens.

According to this diagram, the general types of the resistivity versus temperature graph are exhibiting metallic behavior in the non-superconducting state and can be formulated as $\rho_n(T) = \rho_0 + \beta T$.

In this linear equation, ρ_0 and β are the residual resistivity and the slope of line in the normal state, respectively, where the first term indicates the sample uniformity and the second term represents the essential electronic relationship. The primary decline of resistivity in the transition area is categorized as $T_{C\text{ onset}}$ and shown in Fig. 4. This value is 94.20 K for pure sample, which is 1.5 K higher than the data reported in [37]. Other values are 95.95, 96.41, 96.46, and 95.91 K, from resistivity for samples with SnO₂ nanoparticles addition $x = 0.20, 0.40, 0.50,$ and 0.60 wt %, respectively. These numbers rise when SnO₂ doping upsurge up to $x = 0.50$ wt %. The $T_{C\text{ onset}}$ enhancement is well-defined for SnO₂-doped ($x = 0.50$ wt %) sample which is documented within the inset of Fig. 4 and Table 2.

This behavior is similar when 0.20 wt % quantities of SnO₂ nanoparticles is added to the Y-123 polycrystalline superconductors [12]. Superconducting transition width T_C , which is listed in Table 2, estimated by the $d\rho/dT$ patterns at full width on half-maximum of

the peaks, was about 0.405333 K related to pure Y-358 sample and less than 1 K for samples with SnO₂ addition, indicating a good quality of samples. Increasing the value of ΔT_C by adding of SnO₂ revealed that the grains links depressed [38]. This can be ascribed to oxygen possession of granules in the compound being less uniform due to adding of SnO₂ nanoparticles in YBCO samples as compared to the pure one [39]. There is general consensus in the literature that dimensionality of fluctuation conductivity and the critical and mean-field systems are significantly influenced by non-uniformities and types of superconducting granule [19, 40, 41]. Some of the resistivity is two times larger than that reported for *ab*-plane resistivity of high-purity single crystal Y-123 with the optimum oxygen content at $T_C = 92$ K [42]. The non-superconducting state resistivity decreases with increasing SnO₂ concentration in all samples except for $x = 0.4$ wt %. To describe this decrease it is expected that dissimilar crystallographic alignments and consequently granule border-lines, which influence the electron scattering deficiency factor, are responsible for reduction of resistivity. In non-superconducting state, resistivity is correlated to absorbency, granule border spreading, and its linearity during a slower temperature intermission corroborates the information that the formulation

Table 2. Transition temperature, ρ_0 , ρ_n , and β related to resistivity experimentations for Y-358 specimens with varied quantities of SnO₂ nano-sized insertion

Y-358 + x wt % SnO ₂					
Parameters	x = 0	x = 0.20	x = 0.40	x = 0.50	x = 0.60
$T_{c \text{ onset}}$, K	94.20	95.95	96.41	96.46	95.91
$T_{c \text{ zero}}$, K	88.75529	85.15309	87.80119	85.43792	85.52536
T_C^p , K	93.40267	94.91378	94.97778	95.35822	95.088
ΔT_C , K	0.405333	0.9173334	0.832	0.9173334	0.661334
$\rho_0(0 \text{ K})$, m Ω cm	0.43377	0.32541	0.50492	0.31279	0.39836
$\rho_n(290 \text{ K})$, m Ω cm	0.75578	0.58866	0.81803	0.55279	0.65155
$\beta = d\rho/dt$, $\mu\Omega$ cm/K	1.11	0.907759	1.08	0.827597	0.873067

and manufacture of the compounds are completed properly, for pure and SnO₂-doped YBCO samples.

According to Fig. 4 and its inset, it can be seen that only for sample $x = 0.40$, the electrical resistivity increases as compared with the pure one and for the other samples decrease.

Data related to this matter, $\rho_0(0 \text{ K})$ and $\rho_n(290 \text{ K})$, versus Y-358 + x wt % SnO₂ addition are listed in Table 2.

These outcomes denoted that the entire specimens change to superconductivity state below 85 K. The occurrence of lower resistivity with SnO₂ nanoparticles addition in normal state can be clarified by the equality in the transporter attention because of the oxygen doping balanced and rising the relaxation time due to a less quantity of imperfections, disarray, and non-uniformities whilst the SnO₂ doped upsurges. Figure 5 displays the differentiation of resistivity $d\rho/dT$ graph which has been functioned for the calculation of the critical superconducting temperature T_C .

The temperature corresponding to the peak of this curve defines the critical superconducting temperature T_C^p and is recorded in Table 2. While inclusion of SnO₂ dopant rises up to $x = 0.50$, the critical temperature (T_C^p) is enhanced and suggesting intragranular variations related to the assimilation of tin. The upsurge of T_C for Y-358 with 0.50 wt % SnO₂ nanoparticles inclusion specimen is the biggest value in this research and $x = 0.60$ causes the reduction of T_C to the 95.088 K. However, related to this matter the case of $x = 0.50$ is the optimum value for the critical temperature. Whenever T_C of 0.20 wt % SnO₂-added sample reached 94.91378 K, it could be compared with the T_C of 0.40 wt % SnO₂ nano-sized inclusion specimen and approached nil resistivity by the $T_{C \text{ zero}}$ equivalent to 85.15309 K. This investigation designates that with SnO₂ doped up to 0.50 wt %, the T_C of prepared specimens will increase to 95.35822 K ultimately so

denoted in Fig. 5 accompanied by a middling of $\sim 0.75 \text{ K}$ transition widths.

Figure 6 illustrates a plot of $\ln(\Delta\sigma)$ against $\ln(\epsilon)$ for pure and nano-size SnO₂-doped Y-358 specimens.

This figure aims to associate the experimental data related to conductivity fluctuation $\Delta\sigma$ with the theoretic calculations of excess conductivity. To that effect, every curve exhibited in Fig. 6a might be clearly partitioned into three separate areas, namely, critical fluctuation, Gaussian or mean-field fluctuations, and short-wave fluctuation areas. Critical fluctuation system coupled by $v_{cr} = -0.24502$ related to pure sample, is depicted in Fig. 6a. For doped ones, v_{cr} fit in the $(-0.32547 \leq v_{cr} < -0.24502)$ domain. Polycrystalline [43], single-crystal [44], and thin film [45] are such a materials that this system was also traceable on them. In Gaussian section, the dense streaks signify theoretic equals with -0.5 , -1 , and -1.5 slopes, value for

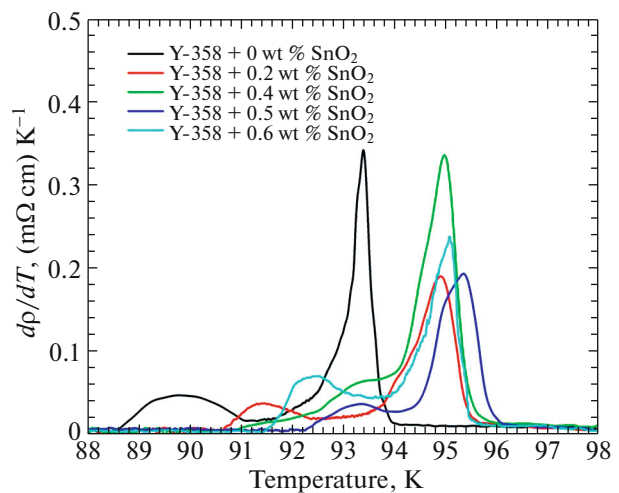


Fig. 5. The differentiation of resistivity conspiracies against temperature of Y-358 specimens mixture with varied amounts of SnO₂ doping.

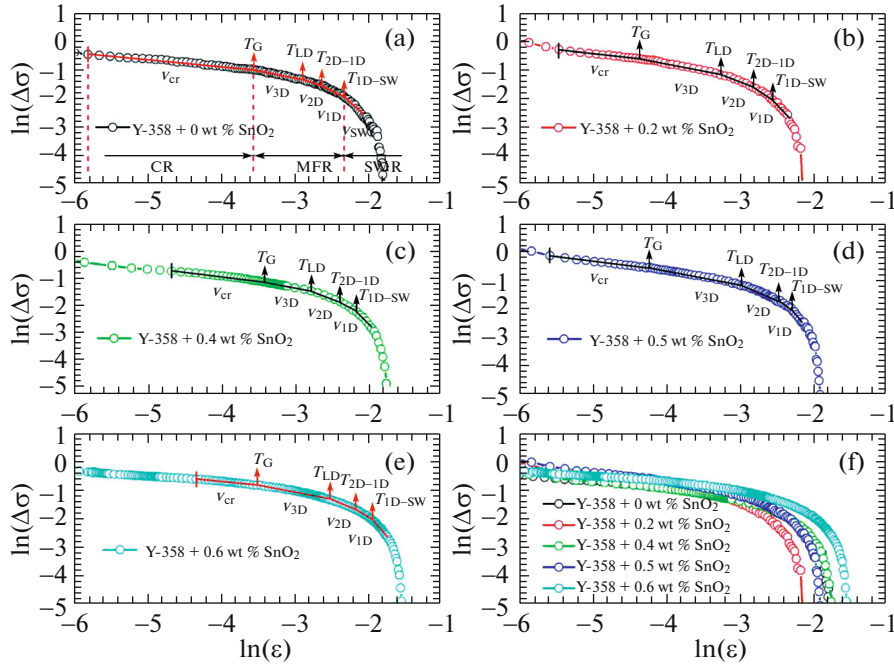


Fig. 6. Graph of $\ln(\Delta\sigma)$ against $\ln(\epsilon)$ of the Y-358 + x wt % SnO_2 nanoparticles addition ($x = 0, 0.20, 0.40, 0.50$, and 0.60) specimens. The dense streaks illustrate v_{cr} ($-0.32547 \leq v_{\text{cr}} \leq -0.24502$ for critical region), the theoretical slopes $-0.5, -1, -1.5$, and -3 on behalf of 3D, 2D, 1D, and SW schemes, respectively. Critical, mean-field, and short-wave regions are denoted by CR, MFR, and SWR symbols, respectively.

three, two, and one dimensionality schemes, respectively. For each sample, these discrete linear segments showing fluctuation conductivity behavior in the Gaussian area ($-4.5 < \ln(\epsilon) < -1$) are exhibited in Figs. 6a to 6e. Altogether, the investigational statistics are depicted in Fig. 6f for easy comparison and quick assessment.

For three-dimensional fluctuations while $v = -0.5$, the intercepts of lined fitting adjust from -2.52269 to -2.8099 and then computed data for $A_{3\text{D}}$ hints to achieve the coherence length alongside the c axis at the zero-Kelvin, $\xi_c(0)$. These data adapts from 12.6333 to 9.47946 Å, related to the Y-358 + x wt % SnO_2 compounds, and recorded in Table 3.

The lowest $\xi_c(0)$ in the sequence is 9.47946 Å at $x = 0.60$. Between these quantities for none-added sample whilst $x = 0$, $\xi_c(0)$ was $\sim 15\%$ superior than the one reported (10.95 Å) for Y-358 pure sample. Nevertheless, by rising nanoparticles SnO_2 addition, $\xi_c(0)$ reduced which designates extra disarray stately of the specimens [19].

For two-dimensional fluctuations while $v = -1$, the intercepts of linear fitting adjust from -4.24894 to -3.81605 and then computed value for $A_{2\text{D}}$ hints to achieve the super layer length d . This value decreases from 106.54 to 69.1055 Å, related to the Y-358 + x wt % SnO_2 ($x = 0$ to 0.60) compounds which named First method (Formula), and its quantities are listed in

Table 3. Junction temperatures between three- and two-dimension border $T_{2\text{D}-3\text{D}}$ are estimated via crossing of the two linear segments and then by the substitution of $T_{2\text{D}-3\text{D}}$ into Eq. (11), the interlayer coupling J is computed, and finally by the substitution of J and $\xi_c(0)$ into Eq. (10), the super layer length d is found and known as Second method (Measured). The value of d varies from 103.831 to 67.2684 Å, versus the Y-358 + x wt % SnO_2 compounds. The quantities regarding both procedures are similar and for comparison, a plot of the super layer length d against SnO_2 addition is depicted for two methods with their average in Fig. 7.

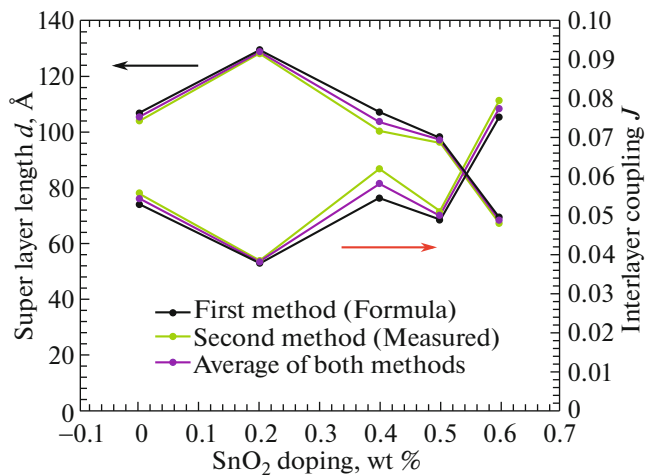
Going over this graph implies that except for $x = 0.20$, by cumulative SnO_2 doping the super layer length d reduces but anisotropy γ upsurge, which is recorded in Table 3. As far as the charge carriers involve, the diminution in quantities related to d can be interpreted as reduction of relaxation time and distressing of their mean free path. The coupling among the CuO_2 planes is effected by the sum of replacement positions which triggers a growth in anisotropy γ with the addition of SnO_2 nanoparticles because the dimension of the Sn ions (0.83 Å), is greater than that of Cu ions (0.68 Å at low spin) [46]. According to AL and LD outline, the total interlayer coupling J changes from 0.05438 to 0.07735 , which specifies no significant movement per atom by increasing SnO_2 addition (see Table 3 and Fig. 7). Diverse temperatures cor-

Table 3. Distinctive factors associated with conductivity fluctuation study on behalf of Y-358 mixtures by altered quantities of SnO₂ nano-sized inclusion. FM (first method), SM (second method), CR (critical region), SW (short wave)

Y-358+ x wt % SnO ₂						
	Parameters	x = 0	x = 0.20	x = 0.40	x = 0.50	x = 0.60
Slope of linear fit for CR	v _{cr}	-0.24502	-0.29258	-0.32547	-0.30938	-0.2657
Intercepts of linear fit	v _{cr}	-1.89069	-1.92925	-2.2406	-1.88977	-1.7312
	v _{3D} = -0.5	-2.8099	-2.80588	-2.799	-2.65682	-2.52269
	v _{2D} = -1	-4.24894	-4.4434	-4.25297	-4.16563	-3.81605
	v _{1D} = -1.5	-5.49518	-5.87772	-5.47378	-5.44995	-4.91305
	v _{sw} = -3	-8.88823	-9.71619	-8.70644	-8.92492	-7.81879
Coherence length	$\xi_c(0)$, Å	12.6333	12.5826	12.4964	10.8402	9.47946
Super layer length <i>d</i> , Å	FM (Formula)	106.54	129.41	106.971	98.0242	69.1055
	SM (Measured)	103.831	128.337	100.344	96.1218	67.2684
Interlayer coupling <i>J</i>	FM (Formula)	0.05298	0.03782	0.05459	0.04892	0.07527
	SM (Measured)	0.05578	0.03845	0.06204	0.05087	0.07943
Anisotropy	γ	0.79156	0.79475	0.80023	0.92249	1.05491

related to their dimensionality fluctuation associated with varied SnO₂ nanoparticles substance are tabulated in Table 4.

Consistent with this Table 4, poorer T_C numbers than T_{LD} signify that the thermodynamically triggered Cooper pairs are produced inside the granule at reasonably higher temperatures but because of the intragranular instabilities, the mean field critical temperature comes down to smaller values. It can be concluded that the three-dimensional Gaussian system controls the 3D boundary for acquiring of superconductivity long-range order in the bulk compound [47].

**Fig. 7.** Plots of *d* and *J* parameters against various addition for the Y-358 added with SnO₂ specimens via twofold approaches and their average.

Close to T_C , once the reduction of temperature occurs, earliest superconductivity is founded in the CuO₂ planes, by way of a 2D establishment, and changeover to a distinct 3D system [48].

The scanning electron microscopy (SEM) images with two magnifying factor 2500 (a, b, c, d, and e) and 10000 (f, g, h, i, and j) related to Y₃Ba₅Cu₈O_{18±δ} + x wt % (x = 0, 0.20, 0.40, 0.50, and 0.60) polycrystalline mixtures with nano-sized SnO₂ doping are shown in Fig. 8.

This figure illustrates that the random orientation of grains and nano-sized tin-oxide inclusions consequence an almost decrease of the grain size in YBCO samples which confirms by the average crystallite size values 50.32623, 44.65428, 46.63808, 51.63545, and 48.48951 nm associated with x = 0, 0.20, 0.40, 0.50, and 0.60, respectively (x = 0.50 is exceptional case). It can be observed that for both sets of images, by increasing the nanoparticles SnO₂, the homogeneity of the samples and also connectivity between the grains is improved. Lower dimensional effects in the transport properties can occur with the decrease in grain size when the number of grain boundaries increases and consequently imply a greater number of weak links (see [49, 50]).

Figure 9 shows scanning electron micrographs of Y₃Ba₅Cu₈O_{18±δ} sample with 0.50 wt % SnO₂ nanoparticles doping with magnification 10000×.

Among the SEM images, the one with x = 0.50 doped has chosen because of the highest value of average crystallite size. In this figure, (a) normal SEM image and (b) modified SEM image related to Fig. 8i are shown, respectively. To compare these two images for better exhibition of particles, the pixels intensity below the minimum threshold value are displayed in

Table 4. SnO₂ nanoparticles substance dependency of various intersect temperatures such as GL, LD, and SW fluctuation accompanied with their temperature range

Y-358+ x wt % SnO ₂					
Parameters	$x = 0$	$x = 0.20$	$x = 0.40$	$x = 0.50$	$x = 0.60$
T_G , K	96.0474	96.11491	98.08827	96.74305	97.91333
T_{LD} , K	98.61253	98.56326	100.86982	100.20938	102.64119
T_{2D-1D} , K	100.20533	100.58491	103.71196	103.40371	105.92503
T_{1D-SWF} , K	102.48136	102.32316	105.92442	104.92568	108.66528
ΔT_{v1D}	2.27603	1.73825	2.21246	1.52197	2.74025
ΔT_{v2D}	1.5928	2.02165	2.84214	3.19433	3.28384
ΔT_{v3D}	2.56513	2.44835	2.78155	3.46633	4.72786

Table 5. Some computed superconducting data related to added and pure Y-358 specimens with different quantities of nano-sized SnO₂ insertions

Y-358+ x wt % SnO ₂					
Parameters	$x = 0$	$x = 0.20$	$x = 0.40$	$x = 0.50$	$x = 0.60$
$B_c(0)(T)$	18.4203	18.49454	18.62217	21.46727	24.5488
$B_{c1}(0)$, T	3.40427	3.41089	3.42221	3.65616	3.87688
$B_{c2}(0)(T)$	206.2026	207.86829	210.74717	280.06216	366.23645
$J_c(0)$, 10 ⁹ A/m ²	1.00267	1.00672	1.01366	1.16853	1.33627
$J_c(0)$, A/cm ²	100267.38658	100671.54933	101366.27917	116852.99501	133626.75237

blue (background contribution), and the pixels intensity above the maximum threshold value are depicted in green colour. However, according to Figs. 9a and 9b, enrichment of granule volume and solidity arrangements while the SnO₂ addition rises is demonstrated at this particular amount ($x = 0.50$). The granules similarly appear to lengthen further at one lateral, creating an almost four-sided pattern with an ordinary size of 1.5 μ m.

From Eqs. (14) to (17), some superconducting parameters such as the critical current density $J_c(0)$ and critical magnetic fields, $B_c(0)$, $B_{c1}(0)$, $B_{c2}(0)$ versus none-added and added specimens are computed and placed in Table 5.

Comparing all the quantities of $B_c(0)$, $B_{c1}(0)$, $B_{c2}(0)$, and $J_c(0)$ for pure and doped Y-358 specimens confirms that by growing the number of nanoparticles of tin-oxide dopant, the mentioned parameters are improved. This situation designates the enhancement of flux pinning effects.

5. CONCLUSIONS

High-temperature polycrystalline Y-358 superconductors have been synthesized via the conventional solid-state reaction route with tin-oxide nanoparticles insertion from $x = 0$ to 0.60 wt % (Y-358 + x wt %

SnO₂). Phase formation and microstructures have been methodically surveyed by XRD and SEM. The X-ray diffraction technique showed the slight variation of the crystal lattice parameters and overall reduction of the orthorhombicity by increasing the content of SnO₂ in YBCO matrix. SEM observations and the crystallite size calculation showed that the grain size and the average crystallite size decreased with rising the amount of SnO₂ in Y-358 specimens as compared to the SnO₂-free sample. The resistivity-temperature graphs obtained by the standard four-point probe method exhibited metallic and superconducting behavior during the normal and superconducting state, respectively, with and without SnO₂ doping. The effect of tin-oxide nanoparticles on the conductivity fluctuation of high-temperature superconductor polycrystalline Y-358 was considered by the AL and LD outlines. Adding SnO₂ to the Y-358 compound causes enhancing some superconducting properties, specifically, T_C in all composites.

SnO₂ addition causes not only structural but also dimensional modifications associated with the mesoscopic and microscopic level of irregularities in the composite. These effects can be interpreted as disarray because of substituting a number of Cu sites into Y-358 which effects some variation in electronic arrange-

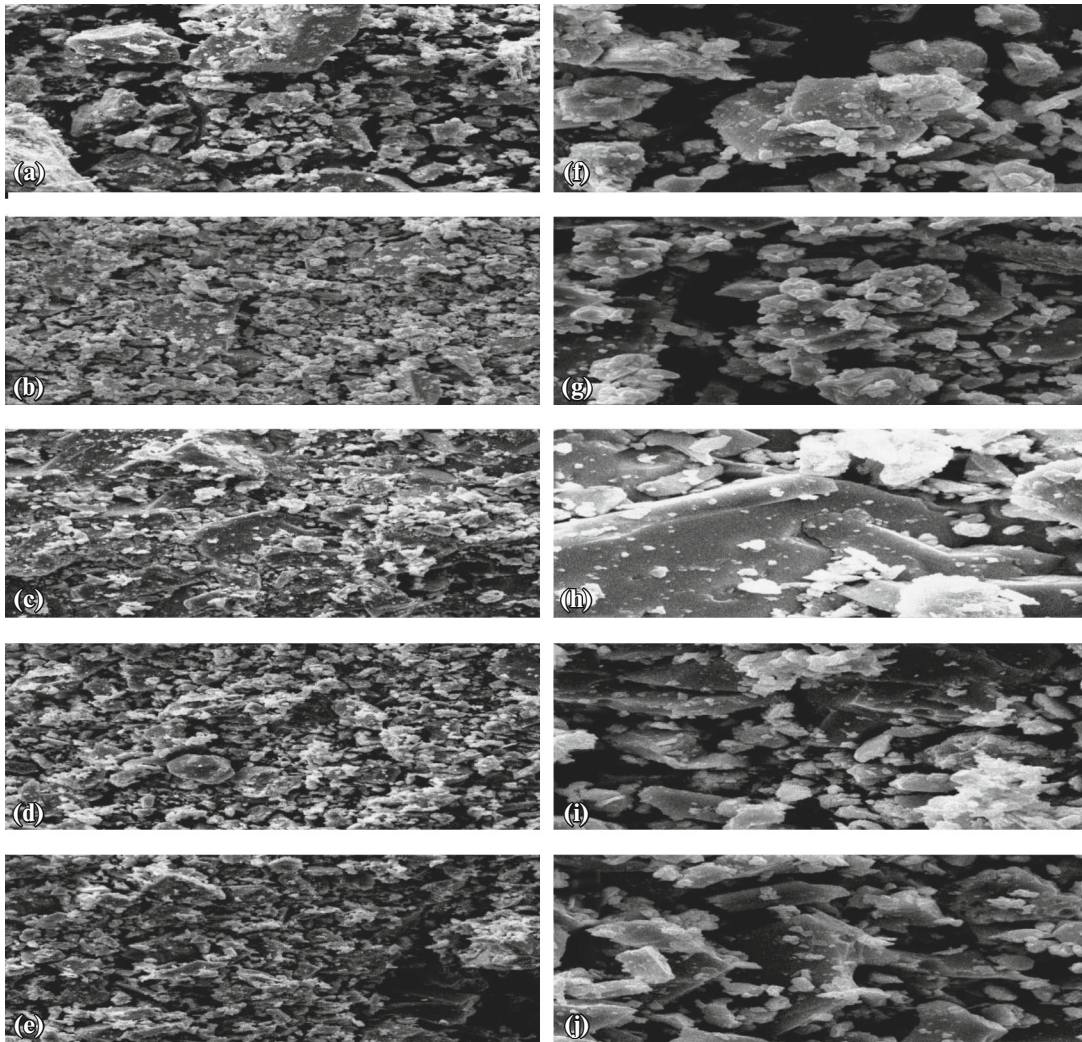


Fig. 8. Scanning electron micrographs of $Y_3Ba_5Cu_8O_{(18 \pm \delta)}$ specimens with 0 (a, f), 0.20 (b, g), 0.40 (c, h), 0.50 (d, i), and 0.60 wt % (e, j) (magnifying factor 2500 and 10000 separately) SnO_2 nano-sized particles added. The random orientation of grains and almost modification of connectivity in several parts is apparent.

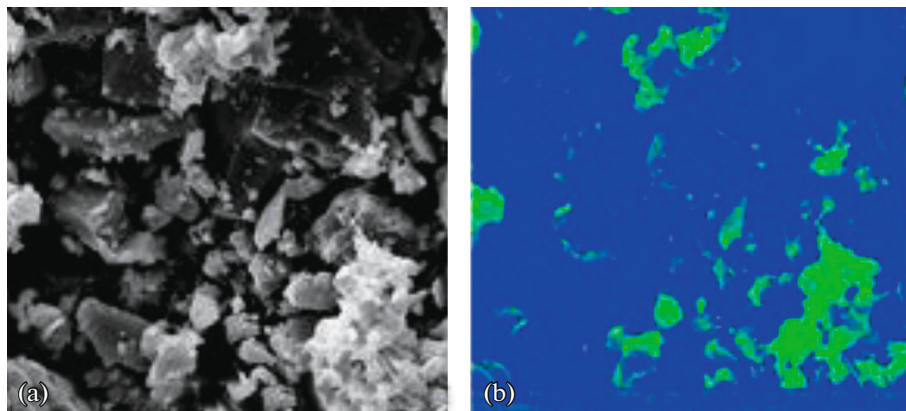


Fig. 9. Scanning electron micrographs of $Y_3Ba_5Cu_8O_{(18 \pm \delta)}$ samples with 0.50 wt % SnO_2 nanoparticles doping with magnification $10000\times$. (a) Normal SEM image, (b) Modified SEM images, the pixels intensity below the minimum threshold value (background contribution) displayed in darker hue (color online: blue), and the pixels intensity above the maximum threshold value depicted in lighter hue (color online: green) for better exhibition of particles.

ment of the granules, and by way of an outcome, the non-existence of an optimized carrier concentration in the CuO_2 flat surfaces. By cumulative SnO_2 inclusions, T_C and anisotropy γ increase but super-layer length d decrease whereas in general interlayer coupling J does not change significantly. These outcomes might be described as the redistribution of charges in the superconducting matrix due to the oxygen content, the number of substitution sites, resistance of the feeble link affected by irregularities, and non-existence of displacement per atom, respectively. Our data showed the conductivity fluctuations, and while the doping level of tin-oxide nanoparticles in Y-358 compounds increased, the critical parameters such as $B_{c1}(0)$, $B_{c2}(0)$, and $J_c(0)$ improved and indicated enhanced flux pinning.

ACKNOWLEDGMENTS

The authors are grateful to Mr Fatemi, for his help during the preparation of the samples and also Mr Kowsari and Mr Nowroozi from Islamic Azad University—Shiraz branch and Mr Mahmoodinezhad from the Brandenburg University of Technology, Germany for their help and valuable comments.

CONFLICT OF INTEREST

The authors declare that they have no conflicts of interest.

REFERENCES

1. D. S. Fisher, M. P. A. Fisher, and D. A. Huse, *Phys. Rev. B* **43**, 130 (1991).
<https://link.aps.org/doi/10.1103/PhysRevB.43.130>
2. P. C. Hohenberg and B. I. Halperin, *Rev. Mod. Phys.* **49**, 435 (1977).
3. C. Biagini, R. Ferone, R. Fazio, F. W. J. Hekking, and V. Tognetti, *Phys. Rev. B* **72**, 134510 (2005).
4. X. M. Cui, G. Q. Liu, J. Wang, Z. C. Huang, Y. T. Zhao, B. W. Tao, and Y. R. Li, *Phys. C (Amsterdam, Neth.)* **466**, 1 (2007).
5. S. N. Abd-Ghani, H. K. Wye, K. Ing, R. Abd-Shukor, and K. Wei, *Adv. Mater. Res.* **895**, 105 (2014).
6. G. Shams and M. Ranjbar, *Braz. J. Phys.* **49**, 808 (2019).
7. G. Shams, A. Mahmoodinezhad, and M. Ranjbar, *Iran. J. Sci. Technol. Trans. A: Sci.* **42**, 2337 (2018).
8. R. Teranishi, Y. Miyanaga, K. Yamada, N. Mori, M. Mukaida, M. Miura, M. Yoshizumi, T. Izumi, M. Namba, S. Awaji, and K. Watanabe, *Phys. C (Amsterdam, Neth.)* **470**, 1246 (2010).
9. S. Choi, G. Shin, and S. Yoo, *Phys. C (Amsterdam, Neth.)* **485**, 154 (2013).
10. Y. Miyanaga, R. Teranishi, K. Yamada, N. Mori, M. Mukaida, T. Kiss, M. Inoue, K. Nakaoka, M. Yoshizumi, T. Izumi, Y. Shiohara, M. Nanba, S. Awaji, and K. Watanabe, *Phys. C (Amsterdam, Neth.)* **469**, 1418 (2009).
11. Z. He, T. Habisreuther, G. Bruchlos, D. Litzkendorf, and W. Gawalek, *Phys. C (Amsterdam, Neth.)* **356**, 277 (2001).
12. N. N. Mohd Yusuf, M. M. Awang Kechik, H. Baqiah, C. Soo Kien, L. Kean Pah, A. H. Shaari, W. N. W. Wan Jusoh, S. I. Abd-Sukor, M. Mousa Dihom, Z. A. Talib, and R. Abd-Sukor, *Materials* **12**, 92 (2019).
13. L. Aslamazov and A. Larkin, in *30 Years of the Landau Institute—Selected Papers* (World Scientific, Singapore, 1996), p. 23.
14. P. Pureur, R. Menegotto-Costa, P. Rodrigues, Jr., J. Kunzler, J. Schaf, L. Ghivelder, J. Campa, and I. Rasines, *Phys. C (Amsterdam, Neth.)* **235–240**, 1939 (1994).
15. X. Tang, Q. Liu, J. Wang, and H. Chan, *Appl. Phys. A* **96**, 945 (2009).
16. K. Yasukochi, T. Ogasawara, Y. Kubota, and J. Maryuama, in *Proceedings of the 12th International Conference on Low Temperature Physics* (Academic, Kyoto, Japan, 1970), p. 178.
17. A. A. Yusuf, A. Yahya, N. A. Khan, F. M. Salleh, E. Marsom, and N. Huda, *Phys. C (Amsterdam, Neth.)* **471**, 363 (2011).
18. N. A. Khan, N. Hassan, M. Irfan, and T. Firdous, *Phys. C (Amsterdam, Neth.)* **405**, 1541 (2010).
19. Y. Slimani, E. Hannachi, M. K. Ben Salem, A. Hamrita, M. Ben Salem, and F. B. Azzouz, *J. Supercond. Novel Magn.* **28**, 3001 (2015).
20. M. Farbod and M. R. Batvandi, *Phys. C (Amsterdam, Neth.)* **471**, 112 (2011).
21. U. Holzwarth and N. Gibson, *Nat. Nanotechnol.* **6**, 534 (2011).
22. R. Teranishi, Y. Miyanaga, K. Yamada, N. Mori, M. Mukaida, M. Inoue, T. Kiss, M. Miura, M. Yoshizumi, T. Izumi, M. Namba, S. Awaji, and K. Watanabe, *J. Phys.: Conf. Ser.* **234** (2) (2010).
23. P. Udomsamuthirun, T. Kruaehong, T. Nilkamjon, and S. Ratreng, *J. Supercond. Novel Magn.* **23**, 1377 (2010).
24. U. Topal, M. Akdogan, and H. Ozkan, *J. Supercond. Novel Magn.* **24**, 2099 (2011).
25. U. Topal and M. Akdogan, *J. Supercond. Novel Magn.* **25**, 239 (2012).
26. A. O. Ayaş, A. Ekicibil, S. K. Çetin, A. Coşkun, A. O. Er, Y. Ufuktepe, T. Fıkrat, and K. Kıymaç, *J. Supercond. Nov. Magn.* **24**, 2243 (2011).
27. A. Aliabadi, Y. Akhavan Farshchi, and M. Akhavan, *Phys. C (Amsterdam, Neth.)* **469**, 2012 (2009).
28. A. Tavana and M. Akhavan, *Eur. Phys. J. B* **73**, 79 (2010).
29. Y. Slimani, E. Hannachi, M. Ben Salem, A. Hamrita, A. Varilci, W. Dachraoui, M. Ben Salem, and F. Ben Azzouz, *Phys. B (Amsterdam, Neth.)* **450**, 7 (2014).
30. A. Kulpa, A. Chaklader, N. Osborne, G. Roemer, B. Sullivan, and D. Williams, *Solid State Commun.* **71**, 265 (1989).
31. Y. Xu, M. Suenaga, J. Taftø, R. Sabatini, A. Moodenbaugh, and P. Zolliker, *Phys. Rev. B* **39**, 6667 (1989).
32. L. Liu, C. Dong, J. Zhang, and J. Li, *Phys. C (Amsterdam, Neth.)* **377**, 348 (2002).

33. A. Ramli, A. H. Shaari, H. Baqiah, C. S. Kean, and M. M. A. Kechik, and Z. A. Talib, *J. Rare Earths* **34**, 895 (2016).
34. A. H. Salama, M. El-Hofy, Y. S. Rammah, and M. Elkhatib, *Adv. Nat. Sci. Nanosci. Nanotechnol.* **6**, 045013 (2015).
35. M. Takahashi, S. Ohkido, and K. Wakita, *Superconductor*, **263** (2010).
36. R. Giri, V. Awana, H. Singh, R. Tiwari, O. Srivastava, A. Gupta, B. Kumaraswamy, and H. Kishan, *Phys. C (Amsterdam, Neth.)* **419**, 101 (2005).
37. A. Ekicibil, S. K. Cetin, A. O. Ayaş, A. Coşkun, T. Firat, and K. Kıymac, *Solid State Sci.* **13**, 1954 (2011).
38. M. M. Dihom, A. H. Shaari, H. Baqiah, N. M. Al-Hada, C. S. Kien, R. S. Azis, M. M. A. Kechik, Z. A. Talib, and R. Abd-Shukor, *Results Phys.* **7**, 407 (2017).
39. P. Vanderbemden, A. Bradley, R. Doyle, W. Lo, D. Astill, D. Cardwell, and A. Campbell, *Phys. C (Amsterdam, Neth.)* **302**, 257 (1998).
40. I. Bouchoucha, F. B. Azzouz, and M. B. Salem, *J. Supercond. Novel Magn.* **24**, 345 (2011).
41. A. A. Aly, N. Mohammed, R. Awad, H. Motaweh, and D. E. S. Bakeer, *J. Supercond. Novel Magn.* **25**, 2281 (2012).
42. G. Shams, J. Cochrane, and G. Russell, *Phys. C (Amsterdam, Neth.)* **363**, 243 (2001).
[https://doi.org/10.1016/S0921-4534\(01\)00938-8](https://doi.org/10.1016/S0921-4534(01)00938-8)
43. M. Sahoo and D. Behera, *J. Mater. Sci. Eng.* **1**, 115 (2012).
44. J. R. Rojas, A. R. Jurelo, R. M. Costa, L. M. Ferreira, P. Pureur, M. T. D. Orlando, P. Prieto, and G. Nieva, *Phys. C (Amsterdam, Neth.)* **341**, 1911 (2000).
45. P. Mayorga, D. Téllez, Q. Madueno, J. Alfonso, and J. Roa-Rojas, *Braz. J. Phys.* **36** (3B), 1084 (2006).
46. R. D. Shannon, *Acta Crystallogr., Sect. A* **32**, 751 (1976).
47. J. Roa-Rojas, D. Téllez, and M. Rojas Sarmiento, *Braz. J. Phys.* **36** (3B), 1105 (2006).
48. A. Kujur and D. Behera, *Thin Solid Films* **520**, 2195 (2012).
49. S. Falahati, F. Saeb, and V. Daadmehr, *Iran. J. Phys. Res.* **9**, 43 (2009).
50. X. L. Wang, J. Horvat, G. D. Gu, K. K. Uprety, H. K. Liu, and S. X. Dou, *Phys. C (Amsterdam, Neth.)* **337**, 221 (2000).